The Na_xMnO_2 Materials Prepared by a Glycine-nitrate Method as Advanced Cathode Materials for Aqueous Sodium-Ion Rechargeable Batteries

Lazar Rakočević[a], Svetlana Štrbac[b], Jelena Potočnik[a], Maja Popović[a], Dragana Jugović[c], Ivana Stojković Simatović[d,*]

[a]INN Vinca, Laboratory of Atomic Physics, University of Belgrade, Mike Alasa 12-14, 11001 Belgrade, Serbia

[b]IHTM-Institute of Electrochemistry, University of Belgrade, Njegoševa 12, 11000 Belgrade, Serbia

[c]Institute of Technical Sciences of SASA, Belgrade, Serbia

[d]Faculty of Physical Chemistry, University of Belgrade, Sudentski trg 12-16, 11158 Belgrade, Serbia

Abstract

Cathodic materials for sodium-ion rechargeable batteries based on Na_xMnO_2 were synthesized by glycine nitrate method and subsequent annealing at high temperatures. Different crystal structures with different morphologies were obtained depending on the annealing temperature: hexagonal layeredα-$Na_{0.7}MnO_{2.05}$ nanoplates were obtained at 850 ^oC, while 3-D tunnel structured $Na_{0.4}MnO_2$ and $Na_{0.44}MnO_2$, both with rod-like morphology, were obtained at 800 ºC and 900 ºC, respectively. The investigations of the electrochemical behavior of obtained cathodic materials in aqueous $NaNO_3$ solution have shown that $Na_{0.44}MnO_2$ obtained at 900 ºC has shown the best battery performance. Its initial discharge capacities are 123.5 mAh/g, 113.2 mAh/g, and 102.0 mAh/g at the high current densities of 1000, 2000 and 5000 mA/g, respectively.

Keywords: aqueous sodium-ion batteries; cathode material; sodium manganese oxide; nanoplates; nanorods.

[*]*Corresponding author: E-mail: ivana@ffh.bg.ac.rs*

1. Introduction

Increasing energy consumption, as well as an increasing concern for the environment, requires the development of renewable energy sources. Among electrochemical energy storage systems, rechargeable batteries, particularly lithium-ion batteries are the most commonly used as the energy source in portable devices and electric vehicles [1,2]. Since lithium is relatively rare on earth but rapidly consumed, it is necessary to find an adequate replacement. Owing to the similar chemical properties of sodium and lithium, but much higher availability, sodium-ion batteries are one of the best candidates to replace lithium-ion batteries [3]. Both types of batteries contain a unique pair of cathode composed of Li or Na ion intercalation material, and an anode composed of carbon material, the performance of which is studied in a half cell [4-6]. In sodium-ion batteries, transition metal (M=Mn, Co, Fe, Ni) oxides or polyanionic compounds containing metal (Fe, Co, Mn, V) and phosphates or sulfates are used as a cathode [4,6], while hard carbon is the most commonly used anode material [5]. Among transition metal oxides, the best candidates as cathodic materials are those with either tunnel or layered structure, which enable a reversible Na^+-ion intercalation/deintercalation without a significant structural change [4,6]. Moreover, it is also necessary to replace traditionally used highly toxic and flammable organic solvents with aqueous electrolytes, which gives rise to a rapid progress of aqueous Li-ion batteries, and most recently of aqueous Na-ion batteries [7-10].

As a potential cathode material in Na-ion rechargeable batteries, different sodium manganese oxides (Na-Mn-O) have recently attracted a lot of attention [11-13]. Depending on sodium to manganese ratio and temperature, a variety of Na-Mn-O compounds can be synthesized, which was reported for the first time in ref. [14]. Namely, several new ternary

oxides of Na_xMnO_2 type were synthesized, in which the ratio of sodium to manganese Na/Mn ≤ 1: $Na_{0.20}MnO_2$, $Na_{0.40}MnO_2$, $Na_{0.44}MnO_2$, $Na_{0.70}MnO_{2+y}$, ($0 \leq y \leq 0.25$) and $NaMnO_2$, the latter two with two allotropes of α and β. In the same paper [14], the phase diagram was given resulting from the stability of these compounds concerning the Na/Mn ratio and temperature.

Na_xMnO_2 compounds with different crystal structure and morphology can be prepared by various methods. For example, hexagonal-layered $Na_{0.7}MnO_{2.05}$ can be prepared by solvothermal synthesis [15]. Tunnel structured $Na_{0.44}MnO_2$with rod-like morphology can be prepared by solid-state synthesis at high temperatures [16], while one-dimensional single-crystalline $Na_{0.44}MnO_2$ nanowires were produced by low-temperature hydrothermal synthesis [17]. Well-defined single-crystalline $Na_{0.44}MnO_2$ nanowires and nanorods were obtained by polymer pyrolysis method and subsequent annealing at higher temperatures [18], while$Na_{0.44}MnO_2$ nanoribbons can be prepared by NaCl-flux reaction at 850 ^oC [19]. Tunnel structured $Na_{0.4}MnO_2$ with well-defined rod-like morphology can be prepared by a conventional solid-state synthesis [14], glycine-nitrate method [20], or through alkaline hydrolysis [21], in all cases followed by annealing at temperatures below 750 ^oC.

The main electrochemical properties of Na-Mn-O cathode materials involve their cycling performance and reversible capacity. The performance of these compounds as the cathode material in Na-ion batteries in both non-aqueous and aqueous electrolytes mainly depends on their crystal structure and morphology. The following research reports relate to the behavior of Na-Mn-O cathode materials in non-aqueous electrolytes (1 M $NaClO_4$ dissolved in a mixture of organic solvents). For instance, layered $Na_{0.7}MnO_2$ nanoplates exhibit a high reversible capacity of 163 mAh/g, and a satisfactory cyclability [22]. Single crystalline tunnel structured $Na_{0.44}MnO_2$ nanowires and nanorods obtained after annealing at 750 ^oC have shown exceptional cyclic

performance (77% capacity retention for 1000 cycles for charge/discharge current density of 60 mA/g), and high reversible capacity of 128 mAh/g for 12 mA/g [18]. $Na_{0.44}MnO_2$ nanoribbons have shown a high capacity of 106 mAh/g, with stable cycling performance [19]. Tunnel structured $Na_{0.4}MnO_2$ nanorods show good cycle performance, and an initial discharge capacity of 83.7 mAh/g at 12mA/g, and maintains 84.7% after 50 cycles [23]. On the other hand, $Na_{0.44}MnO_2$ nanorods synthesized using modified Pechini method shows better rate capability in aqueous (0.5 M Na_2SO_4) than in non-aqueous electrolyte [24]. Research on the behavior of Na-Mn-O cathode materials in aqueous electrolytes has gained momentum only recently, and a brief overview of the latest research will be given. Tunnel structured $Na_{0.4}MnO_2$rods have shown the initial discharge capacity of 38 mAh/g, with good cycling performance in aqueous 1 M $NaClO_4$ solutions [25]. Hexagonal layered $Na_{0.7}MnO_2$ nanoplates have shown an initial specific discharge capacity of 125 mAh/g in 1 M Na_2SO_4 solution during charge/discharge cycling [15]. Finally, the most intensively studied $Na_{0.44}MnO_2$ nanorods have shown the capacity of 80 mAh/g in 3 M $ZnSO_4$ solution [26]. In an aqueous $NaNO_3$ solution (pH = 13.5), the initial capacity was 40 mAh/g [27]. Besides, as the cathode in alkaline Zn-$Na_{0.44}MnO_2$ dual-ion battery, it has shown excellent electrochemical performance with high reversible capacity of 80.2 mAh/g and outstanding cycling stability in 6 M NaOH aqueous electrolyte [28].

In this work, different Na_xMnO_2 powders will be synthesized by glycine-nitrate method (GNM). Such precursor powders will be annealed at three different temperatures: 800 °C, 850 °C, and 900 °C. Na_xMnO_2 compounds with different crystal structures will be obtained, depending on the annealing temperature. X-ray diffraction technique (XRD) will be used for the determination of crystal structure of synthesized powders while scanning electron microscopy with energy-dispersive X-ray spectroscopy (SEM/EDS) will be employed for powders

morphology and elemental analyses. Additionally, chemical analysis including the oxidation state of the obtained compounds constituents will be determined by X-ray photoemission spectroscopy. Electrochemical properties will be tested by cyclic voltammetry and chronopotentiometry in an aqueous $NaNO_3$ solution. Materials obtained by annealing at different temperatures will be compared with each other with a special emphasis on the effect of the structure and morphology on their electrochemical performance (cycling reversibility, efficiency, charge/discharge speed, and specific capacity) for potential use in sodium-ion aqueous batteries.

2. Experimental

2.1. Synthesis of Na_xMnO_2 powders

The synthesis of Na_xMnO_2 powders was performed by the glycine-nitrate method. Aqueous solutions of 2.45 ml 1 M $NaNO_3$ (Merck) and 5.10 ml 0.96 M $Mn(NO_3)_2$ (Merck) were mixed, and then the solid glycine (Merck) was added to the mixture in the molar ratio of 1.2: 1 to nitrate (1.104 g of glycine). The resulting solution was then heated in an oven at 200 °C until the spontaneous combustion. The obtained ash was annealed for four hours at different temperatures: 800 ^oC, 850 ^oC, or 900 ^oC. Thus prepared Na_xMnO_2 powders were further used either for *ex-situ* characterization or the preparation of a working electrode for electrochemical measurements.

2.2. Structural, morphological and chemical characterization of Na_xMnO_2 powders

2.2.1. XRD characterization

Crystal structure and qualitative phase identification of as prepared Na_xMnO_2 powders were analyzed by X-ray diffraction technique using Philips PW-1050 diffractometer with CuKa emission width λ= 0.15418 nm. For all powder samples, data were collected in the 2θ range of 10°–70° with the step of 0.05° and the dwell time of 5s. The analysis of obtained powder patterns was performed by comparison to known powder patterns.

2.2.2. SEM/EDS characterization

Particle morphology and the particle size distribution of as prepared Na_xMnO_2 powders were analyzed using Field emission scanning electron microscopy (FESEM) technique, while chemical composition including surface chemical mapping was analyzed by Energy dispersive spectrometry (EDS) technique, both using FEI SCIOS 2 Dual Beam microscope. The powder was pressed into a copper double-sided adhesive tape to provide mechanical support and electrical contact and then recorded under high vacuum with an accelerating voltage of 10 kV.

2.2.3. XPS measurements

As received Na_xMnO_2 powders were analyzed without any treatment. The powder was pressed onto a copper double-sided adhesive tape to provide mechanical support and electrical contact. Binding energies were corrected using for calibration the position of C1s peak located at 284.8 eV (for adventitious carbon originating from impurities due to exposure to air).

XPS measurements were carried out using the SPECS system with a monochromatic source of X-radiation (AlKα line with photon energy of 1486.3 eV). Survey spectra were recorded in FAT40 mode with step energy of 0.5 eV, and the acquisition time of 0.2 s/channel. High-resolution spectra of the main photoelectron lines for Na, Mn, and O are

recorded in the FAT20 mode with the step energy of 0.1 eV, and the acquisition time of 2 s/channel. The pressure in the analysis chamber was kept at 10^{-8} mbar during the measurements.

2.3. Electrochemical measurements

2.3.1. Working electrode preparation

The suspension for the working electrode was prepared by mixing 85% of the powder sample, 10% of the carbon black (VulcanXC72, Cabot Corp.), and 5% polyvinylidene fluoride (PVDF) in a 2% solution of N-methyl-2-pyrrolidone (Merck). After homogenization in an ultrasonic bath, the suspension was smeared as a thin layer over a glassy carbon electrode (geometric area= 1.2 cm^2) and dried under vacuum for 4 h at the temperature of 140 ^oC. The resulting amount of the material synthesized at 800, 850 or 900 ^oC obtained by subtracting the weight of the bare glassy carbon substrate, were 1.11, 1.23 and 1.36 mg, respectively.

2.3.2. Cyclic voltammetry measurements

Electrochemical characterization was performed using Gamry PCI4/750 in a three-electrode cell consisting of a working electrode, platinum foil as a counter electrode and a saturated calomel electrode (SCE) as a reference electrode. Cyclic voltammograms were recorded in an aqueous 6 M $NaNO_3$ electrolyte in the potential range from -1.30 V to 1.35 V, and using different sweep rates in the range from 20 mV/s to 400 mV/s.

2.3.3. Chronopotentiometry measurements

Chronopotentiometry technique was used for the evaluation of charge/discharge behavior of obtained Na_xMnO_2 electrodes. Measurements were performed using Gamry PCI4/750

potentiostat in saturated aqueous $NaNO_3$solution. Five cycles were recorded for each electrode in the potential range from -1.00 V to 1.25 V, and applying the current densities of 1000, 2000 and 5000 mA/g.

3. Results and discussion

3.1. Crystal structure and morphology of Na_xMnO_2 powders

XRD diffractograms of Na_xMnO_2 powder samples synthesized at 800 ^{0}C, 850 ^{0}C, and 900 ^{0}C are shown in Fig. 1, where each crystallographic plane is labeled by Miller indexes (hkl). Sharp peaks in all XRD patterns indicate that the obtained powders consist of highly crystalline phases, the structure of which differ and depend on the annealing temperature. SEM microphotographs showing the morphology of each obtained Na_xMnO_2 powder samples are also shown in Fig.1.

According to the positions of the reflections in the diffractogram, and when compared to the known reference diffractograms, the powder sample synthesized at 800 ^{0}C, Fig. 1a, is identified as orthorhombic $Na_{0.4}MnO_2$ [JCPDS 27–0749] with a tunnel structure of a romanechite type [14,21]. It was reported earlier that such a structure consists of (3 x 2) tunnels with MnO_6 octahedral units shared by corners and/or edges [14,20,21,23]. Apart from the reflections corresponding to the $Na_{0.4}MnO_2$ compound (marked in red), the ones indicating the presence of impurities as a side product during synthesis are also identified. Among impurities, peaks corresponding to Mn_2O_3 [JCPD 31-0825] [29,30] are observed (marked in blue) as expected from a phase diagram [14], as well as peaks at 37° and 65.6° (marked in black) which are assigned to (121) and (002) crystallographic planes corresponding to α-MnO_2 phase (JCPDS-

72-1982) [31]. SEM micrograph showing the morphology of $Na_{0.4}MnO_2$ powder synthesized at 800 ^{0}C is given in Fig. 1b. Uniformly shaped rod-like structures with the size on a nanometer scale are observed. Such nanorods are 200 to 700 nm long and 60 to 110 nm wide.

The diffraction pattern for powder obtained at 850 ^{0}C, Fig. 1c, corresponds to the reference diffractogram [JCPDS 27-0751] of pure highly crystalline hexagonal-layered α-$Na_{0.7}MnO_{2.05}$ [15,32]. This layered structure is composed of edge-sharing MnO_6 octahedra forming $(MnO_2)_n$ sheets and sodium ions situated between these sheets [15]. Additional reflections, that can also be observed, are ascribed to MnO_2 phase which is indexed to the tetragonal system [JCPDS 72-1982]. SEM microphotographs of $Na_{0.7}MnO_{2.05}$ powder synthesizedat 850 ^{o}C are given in Fig. 1d. It can be seen that the resulting crystalline particles have mostly regular hexagonal-platelet morphology with the size on a nanometer scale. Such hexagonal nanoplates are rather uniform in size with a radius ranging from 500 nm up to 1.5 μm and a thickness ranging from200 nm up to 500 nm.

Powder obtained at 900 ^{0}C, Fig. 1e, is identified as pure highly crystalline orthorhombic $Na_{0.44}MnO_2$ [JCPDS 27-0750], which is in agreement with diffractograms of the same compound reported earlier [16,24,33]. Crystal structure of $Na_{0.44}MnO_2$ is already well described [16,19,24, 27,33], and briefly, it consists of double and triple chains of a rutile type with octahedral MnO_6 molecules on edges and single chains, MnO_5 polyhedrons on edges, and Na situated in tunnels. Its unique tunnel structure is suitable for Na^+ ions intercalation/deintercalation[16,18,24]. SEM micrographs of $Na_{0.44}MnO_2$ powder obtained at 900 ^{0}C is given in Fig. 1f. It can be seen that they are rod-like shaped, with rods approximately a few μm long and few hundred nm wide.

3.2. Chemical analysis of Na_xMnO_2 powders

3.2.1. EDS spectra and the elemental mapping

Chemical analysis of the samples obtained by the mapping technique is shown in Fig. 2. The spatial distribution of the various elements present in the Na_xMnO_2 powders was determined by the elemental mapping. Different colors were used to visually distinguish the presence of sodium (purple), manganese (red) and oxygen (green). Mapping shows that Na, Mn and O are located exactly on those parts of the surface which correspond to the structure seen in the SEM micrographs, which confirms that they consist of these elements. Unlike sodium and oxygen, manganese partly arises out of the surface of the structures visible in SEM micrographs, which originates from Mn at a greater depth due to the higher ability of Mn to reflect electrons as compared to Na and O.

3.2.2. XPS measurements

The survey spectrum of Na_xMnO_2 powders synthesized at different temperatures is given in Fig. 3. The spectrum clearly shows the basic photoelectron and Auger lines of sodium (Na 1s, Na CLL), manganese (Mn2p, Mn LMM), and oxygen (O1s, O-CLL). Besides, the C1s line of carbon, as typical contamination present in each sample is also recorded. It should be noted that the Na Auger lines are located close to the main oxygen line.

High-resolution spectra of Mn2p, Na1s and O1s lines as constitutive elements of each synthesized Na_xMnO_2 powder are given in Fig. 4. To precisely identify the oxidation states of these elements, the spectra are deconvoluted and analyzed. Due to the effect of the spin-orbit coupling Mn2p lines doubled and consists of two components: $Mn2p_{3/2}$ and $Mn2p_{1/2}$. The line $Mn2p_{3/2}$ is fitted using GL(30) pseudo-Voigt profile (30% Lorenzian, 70% Gaussian) with a Shirley background.

For $Na_{0.4}MnO_2$ synthesized at 800 ^oC, Fig. 4a, $Mn2p_{3/2}$ photoelectron line is fitted to three contributions: 641.2 eV, 642.4, and 643.8 eV. In the insets of Fig. 4a, Na1s, and O1s photoelectron lines are presented. Na1s line is fitted to two contributions: 1070.9 eV (marked by 1) and 1072.4 eV (marked by 2), while O1s line is fitted to four contributions: 529.7 eV (marked by 1), 531.3 eV (marked by 2), 532.5 eV (marked by 3) and 533.5 eV (marked by 4). The first Na1s line at lower binding energies corresponds to metal Na, while the second one at higher binding energies corresponds to NaOH following the third O1s peak at 532.5 eV originating from H-O-Na bonding [34,35]. According to literature data [36,37], the first $Mn2p_{3/}2$ peak at 641.2 eV corresponds to either MnOOH (manganite, 641.2 eV in ref. [36], and 641.4 in ref.[37]) or to Mn_2O_3 (640.8 eV in ref. [36], and 641.2 eV in ref. [38]). Since no MnOOH, but rather Mn_2O_3 is positively identified by XRD (see Fig.1), this peak can be ascribed to manganese (III), which is also consistent with the fact that the decomposition of MnOOH into Mn_2O_3 occurs already at 250°C [38]. Besides, this peak is most likely superimposed to the Mn(III) component in pyrolusite (tunnel structured manganese mineral hollandite) [36], and both peaks correspond to the first O1s peak at 529.7 eV. The second and third peaks at 642.4 eV and 643.7 eV, respectively correspond to two components of manganese (IV) multiplet structure as shown in ref. [32]. The one at lower binding energy (also in agreement with 642.5 eV in refs. [36, 38], and 642.2 eV in ref. [39] can be ascribed to MnO_2 following also the first O1s peak [40]. The one at higher binding energies (peaks at 643.5 eV and 644.3 eV in ref. [36]) can be ascribed to Mn(IV) originating from pyrolusite following the secondO1s peak at 531.3 eV for oxygen originating from Na-Mn-O bonding [39]. It should be noted that the fourth O1s line can be ascribed to oxygen from adsorbed water [41], and appears in all investigated Na_xMnO_2 compounds.

For $Na_{0.7}MnO_{2.05}$ synthesized at 850 ^{o}C,Fig. 4b, $Mn2p_{3/2}$ photoelectron line is fitted to two contributions: 642.6 eV, and 644.1 eV. In the insets of Fig. 4b, Na 1s photoelectron line is fitted to two contributions: 1071.9 eV and 1073.9 eV, while O1s line is fitted to four contributions: 530.1 eV (1), 531.7 eV (2), 532.8 eV (3) and 534.1 eV (4). $Mn2p_{3/2}$ photoelectron lines can be ascribed to two Mn(IV) contributions in birnessite (layer structured manganese mineral) [36], and correspond with the first and second O1s lines, respectively. Like in the previous case, the first Na1s lines ascribed to metal Na and the second to NaOH following the third O1s peak[34].

For $Na_{0.44}MnO_2$ synthesized at 900 ^{o}C, Fig. 4c, $Mn2p_{3/2}$ line is fitted to three contributions: 641.2 eV, 642.4, and 643.7 eV, which are equal or very close to the values obtained for $Na_{0.4}MnO_2$ synthesized at 800 ^{o}C, meaning that the peaks correspond to Mn(III) and two Mn(IV) contributions, respectively. In the insets of Fig. 4c, Na 1s photoelectron line is fitted to only one contribution at 1071.9 eV corresponding to metal Na meaning that no traces of NaOH are observed after the annealing at 900^{o}C. O1s line is fitted to three contributions: 530.0 eV (1), 531.5 eV (2), and 534.0 eV (4), which are in agreement with binding energies as in the case of $Na_{0.4}MnO_2$, and can be interpreted in the same way.

3.3. Electrochemical behavior of Na_xMnO_2 in aqueous electrolyte

3.3.1. Cyclic voltammetry of Na_xMnO_2 electrodes

The electrochemical behavior of all prepared Na_xMnO_2 electrodes was investigated by cyclic voltammetry in a saturated aqueous $NaNO_3$ solution.Cyclic voltammograms (CVs) were recorded during continuous cycling of the potential with a sweep rate of 20 mV/s. CVs for Na_xMnO_2 synthesized at 800 ^{0}C, 850 ^{0}C, and 900 ^{0}C are given in Fig. 5.

In all CVs, cathodic peaks corresponding to the process of Na^+-ions intercalation, as well as anodic peaks corresponding to the process of Na^+-ions deintercalation can be observed. The electrochemical reaction of Na^+ intercalation/deintercalation on the cathode can be expressed as [4]:

$$Na_xMnO_2 \leftrightarrow Na_{x-y}MnO_2 + yNa^+ + ye^-,$$

where: x is the number of inserted Na^+ ions. Cathodic peaks correspond to the formation of $Na_{x-y}MnO_2$, while anodic peaks correspond to the initial Na_xMnO_2.

The number, shape, position, and intensity of various cathodic/anodic peaks indicate that there are various processes of Na^+-ions intercalation/deintercalation, which take place in many electrochemical steps. The shape of CVs for all different Na_xMnO_2 electrodes synthesized at different temperatures is changing during cycling.

For each Na_xMnO_2 electrode, independent of the synthesis temperature, cyclic voltammetry shows at least three pairs of reversible cathodic and anodic peaks (I, II and III). The most pronounced peaks (I and III) are most likely associated with the processes of reversible Na^+-ions intercalation/deintercalation, while the peak II, as being not well defined can be associated with the Na^+ vacancies rearrangement during intercalation/deintercalation processes [42]. Apart from that, the sharpness of peaks I and III also tells about the crystalline structure of obtained powders.

For $Na_{0.4}MnO_2$ synthesized at 800 ^{0}C, Fig. 5a, the cathodic and anodic positions of peaks I and II change only slightly during cycling from (0.30 V/ 0.02 V for peak I and 0.96 V/ 1.14 V for peak III) in the first cycle to (0.34 V/0.01 V for peak I and 0.98 V/1.16 V for peak III) in the tenth cycle. This indicates good cycling reversibility of the processes corresponding to the Na^+

ions intercalation/deintercalation. Besides, the intensity of each peak increases with continuing cycling.

The shape of CV for $Na_{0.7}MnO_{2.05}$ synthesized at 850 ^{0}C, Fig. 5b, is changing rapidly after the first cycle showing much higher current densities in the whole potential region. A significant change is observed in the peak I, where its cathodic part at -0.7 V, which is particularly pronounced in the first cycle, decreases and finally disappears up to the tenth cycle. At the same time, a new cathodic peak arises at approx. -0.4 V, and increases up to the tenth cycle. Besides, the first anodic peak at approx. 0.01 V increases significantly after the first cycle, but then decreases with further cycling. These changes which were described as the initial electrode activation similarly like in the case of $Na_{0.6}MnO_2$ [42], can be attributed to the phase transition from $Na_{0.7}MnO_{2.05}$ to $Na_{0.9}MnO_{2.05}$ [15]. After the tenth cycle, the shape of CVs stabilizes, and positions of cathodic and anodic parts of peaks I and III (0.37 V/-0.01 V, and (-0.98 V/1.3 V), as well as their intensity change negligible.

In CVs of $Na_{0.44}MnO_2$ synthesized at 900 ^{0}C, Fig. 5c, starting from the first up to the tenth cycle, the positions of cathodic and anodic parts of peaks I (-0.3 V/0.07 V) and III (0.97 V/1.1 V), are only slightly changed during cycling. Since these peaks correspond to the Na^+ ions intercalation/deintercalation processes there is a good cycling reversibility. On the other hand, the intensities of both cathodic and anodic peaks increase significantly during cycling indicating the improvement in charge/discharge capacity, most likely due to the phase transition to $Na_{0.33}MnO_2$, which occurs in 0.01 M $NaNO_3$ aqueous electrolyte as reported in ref. [43].

Cyclic voltammograms of the same Na_xMnO_2 electrodes, recorded under the same conditions but with different sweep rates ranging from 20 to 400 mV/s, are given in Fig. 6 (a,d,g). For comparison, the current density scales, as well as potential scales are the same in all

cases. For each Na_xMnO_2 electrodes, the shapes of CVs concerning peak positions are similar for all sweep rates. Current densities are similar for $Na_{0.4}MnO_2$ synthesized at 800 ^{0}C, Fig. 6a, and $Na_{0.7}MnO_{2.05}$ synthesized at 850 ^{0}C, Fig. 6d, and increase in a similar extent with increasing sweep rate. On the other hand, current densities for $Na_{0.44}MnO_2$ synthesized at 900 ^{0}C, Fig. 6g, increase much more with increasing sweep rate, meaning that the reversibility of Na^+ ions intercalation/deintercalation is maintained even for higher charge/discharge rates.

CV curves at different current rates were used to analyze the electrochemical kinetics of synthesized materials. The area of a CV curve slowly increased, with the reduction and oxidation peaks shifted to lower and higher voltages, respectively. The ratio of capacitive and faradaic processes can be determinated based on the value of the constant *b* obtained from equation [25, 26, 44] $i = av^b$ where *a* and *b* are adjustable values. The value of b~0.5 is characteristic for the full diffusion-controlled process, while b~1 is characteristic for the full capacitive controlled process. The constant *b* was calculated as the slope of the log (*i*) vs. log (*v*) plots, Fig 6 (b,e,h). For all samples, the value of *b* indicates that the corresponding redox reactions during the charge and discharge processes were combined capacitive and intercalation reactions [25]. For $Na_{0.44}MnO_2$, *b* was the smallest and its values for discharge and charge process were 0.63 and 0.71, respectively, which suggested more favored diffusion kinetics of $Na_{0.44}MnO_2$. The percentage of capacitive and diffusion contribution is determinated by the following equation [26, 44] $i(v) = k_1v + k_2v^{1/2}$ where k_1 and k_2 are constants. The k_1v and $k_2v^{1/2}$ represent the capacitive and the diffusion controlled contribution, respectively. For all samples, with the increase of the scan rate, the diffusion contribution decreased, while the capacitive contribution increased, Fig. 6 (c,f,i). Accordingly, the capacitive contribution of $Na_{0.44}MnO_2$ at scan rate of 50 mV/s was 48.1% and up to 72.5% at 400 mV/s, Fig. 6 (i). A similar ratio of the capacitive and

diffusion contribution was observed with $Na_{0.7}MnO_{2.05}$, while in the case of $Na_{0.4}MnO_2$, even at lower scan rates, the capacitive contribution was over 90%.

Specific capacity was calculated from cyclic voltammograms recorded using a sweep rate of 20 mV/s as the area of the reduction peaks. The initial discharge capacity of $Na_{0.4}MnO_2$ in $NaNO_3$ solution is 50 mAh/g, while after 15^{th} cycle its values increased for 9%. During cycling, material has demonstrated great efficiency (the ratio of the charge/discharge capacity) amounting to ~ 95%.For $Na_{0.7}MnO_{2.05}$ synthesized at 850 ^{0}C, the initial discharge capacity (after the first ten cycles during which the electrode was activated [15,42]) was 75 mAh/g. After an additional ten cycles, the capacity was increased to 79 mAh/g, or for 5%. During cycling, $Na_{0.7}MnO_{2.05}$ has also shown very good efficiency of 97%. The initial discharge capacity for $Na_{0.44}MnO_2$ synthesized at 900 ^{0}C was 46 mAh/g, which after ten cycles was increased to 119 mAh/g, or for 158%. $Na_{0.44}MnO_2$ has also shown very good efficiency of 96%.

Since among investigated electrodes, $Na_{0.44}MnO_2$ synthesized at 900 ^{0}C has shown the best cycling reversibility and specific capacity, its charge/discharge behavior will be examined in more details by chronopotentiometry.

3.3.2. Charge/discharge behavior for $Na_{0.44}MnO_2$ sinthesized at 900 ^{0}C determined using chronopotentiometry technique

Chronopotentiometry measurements were performed for $Na_{0.44}MnO_2$ electrode synthesized at 900 ^{0}C in a saturated aqueous $NaNO_3$ solution, and the obtained results are presented in Fig. 7.

Charge/discharge curves for the first cycle are presented in Fig. 7a.The specific capacities were calculated from these curves by multiplying the discharge times with each applied current

density, t(s) x j(mA/g), Fig. 7b. For the current densities of 1000, 2000, and 5000 mA/g, the calculated discharge capacities were: 123.5, 113.2, and 102.0 mAh/g, respectively. After the 5th cycle, the discharge capacities were slightly increased for all current rates, and the obtained values for the current densities of 1000, 2000, and 5000 mA/g were 123, 113 and 102 mAh/g, respectively. The discharge capacity is practically only slightly changed at very high current densities, which indicates the superiority of the pseudo-capacitance in the total charge storage behavior [26,44]. Furthermore, the same was confirmed based on the appearance of different discharge/charge voltage profiles of $Na_{0.44}MnO_2$ in aqueous and non-aqueous solution [27].

Results show that for $Na_{0.44}MnO_2$ electrode obtained at 900 ^{0}C, with increasing current density, the charging and discharging processes slow down, while the capacity increases. Therefore, this electrode is suitable for sodium-ion intercalation/deintercalation and eligible as a cathode for Na-ion batteries.

4. Conclusion

Na_xMnO_2 powders were synthesized by glycine nitrate method (GNM), and subsequent annealing at three different temperatures: 800 ^{o}C, 850 ^{o}C, and 900 ^{o}C. Detailed structural, morphological and chemical analysis has been performed, as well as the investigation of their electrochemical performance for a potential use as cathodic materials for sodium-ion rechargeable batteries.

By X-ray diffraction analysis has confirmed the crystalline structure of obtained powders identified as: $Na_{0.7}MnO_{2.05}$ with a layered structure, which was obtained at 850 ^{o}C, and tunnel structured $Na_{0.4}MnO_2$ and $Na_{0.44}MnO_2$ nanorods with different morphology, which were obtained at 900 ^{o}C and 900 ^{o}C, respectively.

SEM microscopy have shown that obtained powders have different morphology. Namely, layer structured $Na_{0.7}MnO_{2.05}$ consists of nanoplatets with the average diameter of several micrometers, and the average width of several hundred nanometers. Tunnel structured $Na_{0.4}MnO_2$ consists of nanorods 200 to 700 nm long and 60 to 110 nm wide, while $Na_{0.44}MnO_2$ consists of much larger nanorods, approximately one micron long and few hundred nanometers wide. Surface elemental mapping have shown the distribution of Na, Mn and O as the identified elements. The chemical compositions of the samples and the oxidation state of Na, Mn and O in each powder sample were identified by XPS technique.

The electrochemical behavior of obtained powders has been investigated by cyclic voltammetry and chronopotentiometry. Since$Na_{0.44}MnO_2$ synthesized at 900 ^oC exhibits the best properties concerning capacity and stability, it would be chosen as the best candidate for a cathode in sodium-ion batteries.

Acknowledgement: The work was supported by the Ministry of Education, Science and Technological Development, Republic of Serbia.

References

[1] Y. Liang, C-Z Zhao, H. Yuan, Y. Chen, W. Zhang, J-Q Huang, D. Yu, Y. Liu, M-M. Titirici, Y-L Chueh, H. Yu, Q. Zhang, A review of rechargeable batteries for portable electronic devices,*InfoMat,* 1 (2019) 6-32.

[2] F. Wu, J. Maier, Y. Yu, Guidelines and trends for next-generation rechargeable lithium and lithium-ion batteries,*Chemical Society Reviews*, 49 (2020) 1569-1614.

[3] J.Y. Hwang, S.T. Myung, Y.K. Sun, Sodium-ion batteries: present and future, *Chemical Society Review*s, 46 (2017) 3529-3614.

[4] X. Xiang, K. Zhang, J. Chen, Recent Advances and Prospects of Cathode Materials for Sodium-Ion Batteries, *Advanced Materials*, 27 (2015) 5343-5364.

[5] W. Zhang, F. Zhang, F. Ming, H.N. Alshareef, Sodium-ion battery anodes: Status and future trends, *EnergyChem*, 1 (2019) 100012.

[6]X. Pu, H. Wang, D. Zhao, H. Yang, X. Ai, S. Cao, Z. Chen, Y. Cao, Recent progress in rechargeable sodium-ion batteries: toward high-power applications, *Small,* 15 (2019) 1805427.

[7] J. Liu, C. Xu, Z. Chen, S. Ni, Z.X. Shen, Progress in aqueous rechargeable batteries, *Green Energy & Environment*, 3 (2018) 20-41.

[8]D. Bin, F. Wang, A. G. Tamirat, L. Suo, Y. Wang, C. Wang,Y. Xia, Progress in aqueous rechargeable sodium-ion batteries, *Advanced Energy Materials,* 8 (2018) 1703008.

[9]R. Demir-Cakan, M. Rosa Palacin, L. Croguennec, Rechargeable aqueous electrolyte batteries: from univalent to multivalent cation chemistry, *Journal of Materials Chemistry A*, 7 (2019) 20519-20539.

[10] M. Liu, H. Ao, Y. Jin, Z. Hou, X. Zhang, Y. Zhu, Y. Qian, Aqueous rechargeable sodium ion batteries: developments and prospects,*Materials Today Energy,*17 (2020) 100432.

[11] M. Xu, Y.Niu, Y. Li, S. Bao, C.M Li, Synthesis of sodium manganese oxides with tailored multi-morphologies and their application in lithium/sodium-ion batteries, *RSC Advances*, 4 (2014) 30340-30345.

[12] R.J. Clément, P.G. Bruce, C.P. Grey, Review - manganese-based P2-type transition metal oxides as sodium-ion battery cathode materials, *Journal of The Electrochemical Society*, 162, (2015) A2589-A2604.

[13] K. Kubota, N. Yabuuchi, H. Yoshida, M. Dahbi, S. Komaba, Layered oxides as positive electrode materials for Na-ion batteries, *Materials Research Bulletin*, 39 (2014) 416-422.

[14] J.P. Parant, R. Olazcuaga, M. Devalette, C. Fouassier, P. Hagenmuller, Sur quelques nouvelles phases de formule Na_xMnO_2 ($x \leq 1$), *Journal of Solid State Chemistry*, 3 (1971) 1-11.

[15] Y. Hou, H. Tang, B. Li, K. Chang, Z. Chang, X.-Z. Yuan, H. Wang, Hexagonal-layered $Na_{0.7}MnO_{2.05}$ via solvothermal synthesis as an electrode material for aqueous Na-ion supercapacitors, *Materials Chemistry and Physics*, 171 (2016) 137-144.

[16] F.Sauvage,L. Laffont, J.-M. Tarascon, E. Baudrin, Study of the Insertion/Deinsertion Mechanism of Sodium into $Na_{0.44}MnO_2$, *Inorganic Chemistry*, 46 (2007) 3289-3294.

[17] E. Hosono, H. Matsuda, I. Honma,S. Fujihara,M. Ichihara,H. Zhou, Synthesis of single-crystalline electro-conductive $Na_{0.44}MnO_2$ nanowires with high aspect ratio for the fast charge-discharge Li-ion battery, *Journal of Power Sources,* 182, (2008) 349-352.

[18] Y. Cao, L. Xiao, W. Wang, D. Choi , Z. Nie, J. Yu, L.V. Saraf, Z. Yang, J. Liu, Reversible sodium ion insertion in single-crystalline manganese oxide nanowires with long cycle life, *Advanced Materials*, 23 (2011) 3155-3160.

[19] L. Zhao, J. Ni, H. Wang, L. Gao, Flux synthesis of $Na_{0.44}MnO_2$ nanoribbons and their electrochemical properties for Na-ion batteries, *Functional Materials Letters*, 6 (2013) 1350012

[20] F. Hu, M. Doeff, Electrochemical characterization of manganese oxide cathode materials based on $Na_{0.4}MnO_2$, *Journal of Power Sources,* 129 (2004) 296-302.

[21] S. Liu, C-Z. Fan, Y. Zhang, C-H. Li, X-Z. You, Low-temperature synthesis of $Na_2Mn_5O_{10}$ for supercapacitor applications, *Journal of Power Sources,* 196 (2011) 10502-10506.

[22] D. Su, C. Wang, H-J Ahn, G. Wang, Single Crystalline $Na_{0.7}MnO_2$ nanoplates as cathode materials for sodium ion batteries with enhanced performance, *Chemistry A Europian Journal* 19, (2013) 10884-10889.

[23] Y. Zhang, Z. Liu, H. Deng, J. Xie, J. Xia, S. Nie, W. Liu, L. Liu, X. Wang, Rectangular tunnel-structured $Na_{0.4}MnO_2$ as a promising cathode material withstanding a high cutoff voltage for Na-ion batteries, *ChemElectroChem* 2019, *6*, 1–12.

[24] D.J. Kim, R. Ponraj, A.G. Kannan, H.W. Lee, R. Fathi, R. Ruffo, C.M. Mari, D.K. Kim, Diffusion behavior of sodium ions in $Na_{0.44}MnO_2$ in aqueous and non-aqueous electrolytes. *Journal of Power Sources*, 244 (2013) 758-763.

[25]. M.S. Chae, A. Chakraborty, S. Kunnikuruvan, R. Attias, S. Maddakuri, Y. Gofer, D.T. Major, D. Aurbach, Vacancy-driven high rate capabilities in calcium-doped $Na_{0.4}MnO_2$ Cathodes for Aqueous Sodium-Ion Batteries, *Advanced Energy Materials*, (2020) 2002077.

[26] J. Li, L. Li, H. Shi, Z. Zhong, X. Niu, P. Zeng, Z. Long, X. Chen, J. Peng, Z. Luo, X. Wang, S. Liang, Electrochemical energy storage behavior of $Na_{0.44}MnO_2$ in aqueous zinc-ion battery, *ACS Sustainable Chemistry & Energy*, 8 (2020) 10673-10681.

[27] Y. Wang, J. Liu, B. Lee, R. Qiao, Z. Yang, S. Xu, X. Yu, L. Gu, Y-S. Hu, W. Yang, K. Kang, H. Li, X-Q. Yang, L. Chen, X. Huang, Ti-substituted tunnel-type $Na_{0.44}MnO_2$ oxide as a negative electrode for aqueous sodium-ion batteries, *Nature Communications,* 6 (2015) 1-10.

[28] H. Li, S. Liu, T. Yuan, B. Wang, P. Sheng, L. Xu, G. Zhao, H. Bai, X. Chen, Z. Chen, Y. Cao, Electrochemical mechanism of $Na_{0.44}MnO_2$ in alkaline aqueous solution, *Acta Physico-Chimica. Sinica*36 (2020), 1905027.

[29] National Bureau of Standards, *Standard X-ray diffraction powder patterns*, 539 (1959) 37.

[30] J. Du, G. Xiao, Y. Xi, X. Zhu, F. Su, S.H. Kim, Periodate activation with manganese oxides for sulfanilamide degradation. *Water Research,* 169 (2020) 115278.

[31] Z.Y Leong, H.Y. Yang, A study of MnO_2 with different crystalline forms for pseudocapacitive desalination,*ACS Applied Materials & Interfaces,* 11 (2019) 13176-13184.

[32] S. Patoux, M. Dollé, M.M. Doeff, Layered manganese oxide intergrowth electrodes for rechargeable lithium batteries. 2. Substitution with Al, *Chemistry of Materials*, 20 (2005) 1044–1054.

[33] X. He, J. Wang, B. Qiu, E. Paillard, C. Ma, X. Cao, H. Liu, M. C. Stan, H. Liu, T. Gallash, Y.S. Meng, J. Li, Durable high-rate capability $Na_{0.44}MnO_2$ cathode material for sodium-ion batteries, *Nano Energy*, 27 (2016) 602–610.

[34] A. Barrie, F.J. Street, An Auger and X-ray photoelectron spectroscopic study of sodium metal and sodium oxide, *Journal of Electron Spectroscopy and Related Phenomena*, 7 (1975) l-31.

[35] P.H. Citrin, High-resolution X-ray photoemission from sodium metal and its hydroxide, *Physical Review B,* 8 (1973) 5545-5556.

[36] M.C. Biesinger, B.P. Payne, A.P. Grosvenor, L.W.M. Lau, A.R. Gerson, R.St.C. Smart, Resolving surface chemical states in XPS analysis of first-row transition metals,oxides, and hydroxides: Cr, Mn, Fe, Co and Ni, *Applied Surface Science* 257 (2011) 2717–2730.

[37] H.W. Nesbitt, D. Banerjee, Interpretation of XPS Mn(2p) spectra of Mn oxy-hydroxides and constraints on the mechanism of MnO_2 precipitation, *American Mineralogist,* **83** (1998) 305.

[38] M. Oku, K. Hirokawa, X-ray photoelectron spectroscopy of manganese-oxygen systems, *Journal of Electron Spectroscopy and Related Phenomena,* 7 (1975) 465-473.

[39] H. Lin, D. Chen, H. Liu, X. Zou, T. Chen, Effect of MnO_2 Crystalline structure on the catalytic oxidation of formaldehyde, *Aerosol and Air Quality Research*, 17 (2017) 1011–1020.

[40] M. Oku, X-ray photoelectron spectra of $KMnO_4$ and K_2MnO_4 fractured in situ, *Journal of Electron Spectroscopy and Related Phenomena*, 74 (1995) l35-148.

[41] Z. Shuxian , W.K. Hall, G. Ertl, H. Knozinger, X-ray photoemission study of oxygen and nitric oxide adsorption on MoS_2, *Journal of Catalysis*, 100 (1986) 167-175.

[42] T.R. Chen, Z-G. Wu, W. Xiang, E-H. Wang, C-J. Wu, M-Z. Chen, X-D. Guo, B-H. Zhong, The influences of sodium sources on the structure evolution and electrochemical performances of layered-tunnel hybrid $Na_{0.6}MnO_2$ cathode, *Ceramics International*, 43 (2017) 6303-6311.

[43] F. Sauvage, E. Baudrin, J-M. Tarascon, Study of the potentiometric response towards sodium ions of $Na_{0.44-x}MnO_2$ for the development of selective sodium ion sensors, *Sensors and Actuators B,* 120 (2007) 638–644.

[44] C. Choi, D.S. Ashby, D.M. Butts, R.H. DeBlock, Q. Wei, J. Lau, B. Dunn, Achieving high energy density and high power density with pseudocapacitive materials. *Nature Review Materials,* 5 (2020) 5–19.

Figure Captions

Fig. 1. XRD difractograms (left column) and corresponding SEM micrographs magnified 20000 times (right column) of Na_xMnO_2 powders synthesized at: a,b) 800 ^{0}C; c,d) 850 ^{0}C; e,f) 900 ^{0}C.

Fig. 2.EDS elemental mapping images of Na_xMnO_2 powders synthesized at 800 ^{o}C, 850 ^{o}C, and 900 ^{o}C.

Fig. 3. Survey XPS spectrum of Na_xMnO_2 powder.

Fig. 4. High resolution spectra of $Mn2p_{3/2}$, Na1s and O1s lines for Na_xMnO_2 powders synthesized at: a) 800 ^{o}C; b) 850 ^{o}C; c) 900 ^{o}C.

Fig. 5. CVs of Na_xMnO_2 electrodes synthesized at different temperatures: a) 800 ^{0}C; b) 850 ^{0}C; c) 900 ^{0}C. CVs were recorded in saturated aqueous $NaNO_3$ during continuous cycling with a sweep rate of 20 mV/s.

Fig. 6. Comparison of electrochemical performance of of Na_xMnO_2 synthesized at different temperatures: (a, d, g) cyclic voltammograms recorded in saturated aqueous $NaNO_3$ with different sweep rates within the range of 20-400 mV/s, (b, e, h) log(*i*) vs log(*v*) plots at specific peak currents, and (c, f, i) the average contribution ratio of diffusion and capacitive controlled process.

Fig. 7. Chronopotentiometry results for $Na_{0.44}MnO_2$ electrodes synthesized at 900 ^{0}C obtained for the current rates of 1000, 2000, and 5000 mA g^{-1} in saturated aqueous $NaNO_3$: a) charge/discharge curves; b) discharge capacity vs. number of cycles.

Figure 1

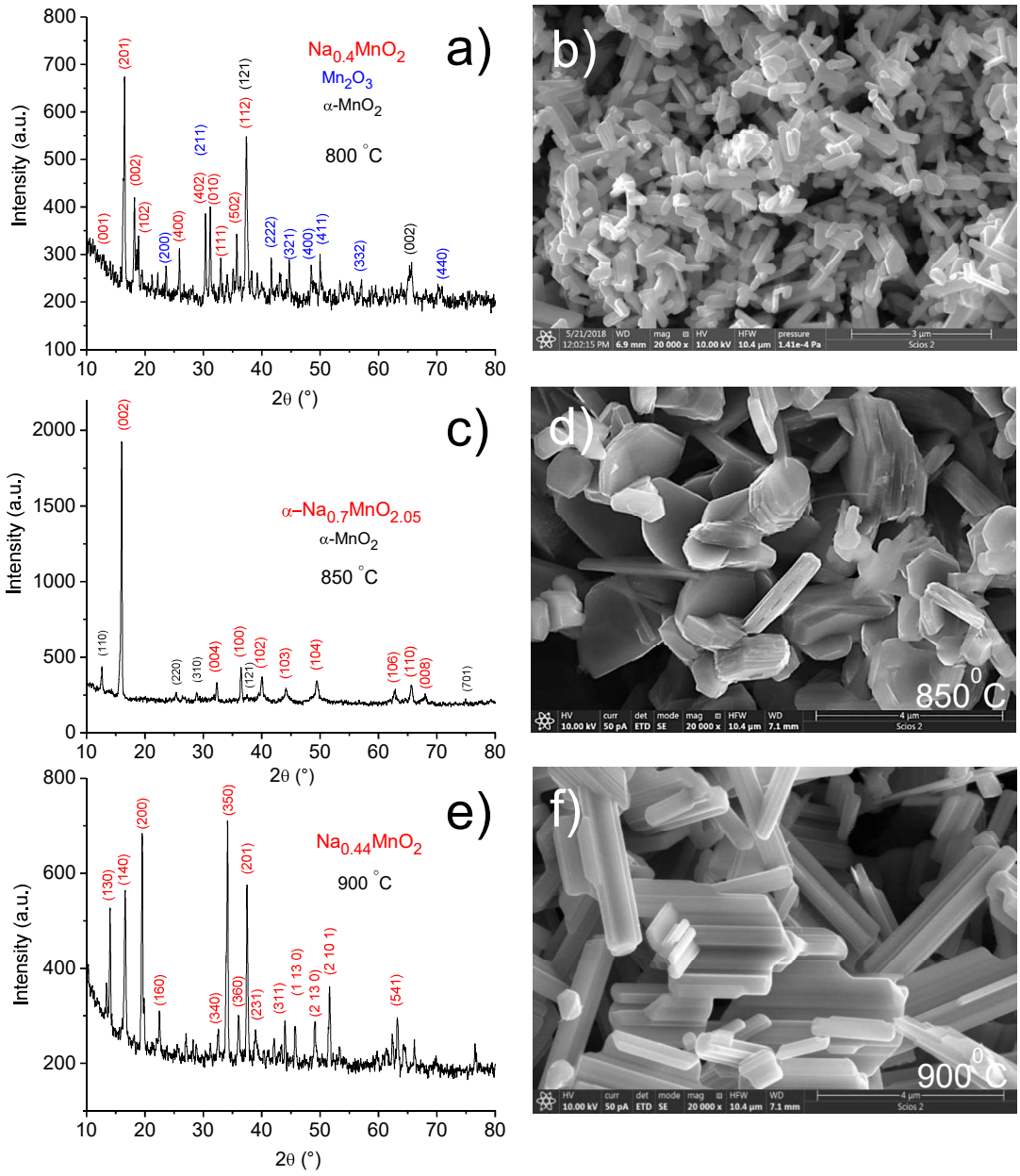

Fig. 1

Figure 2

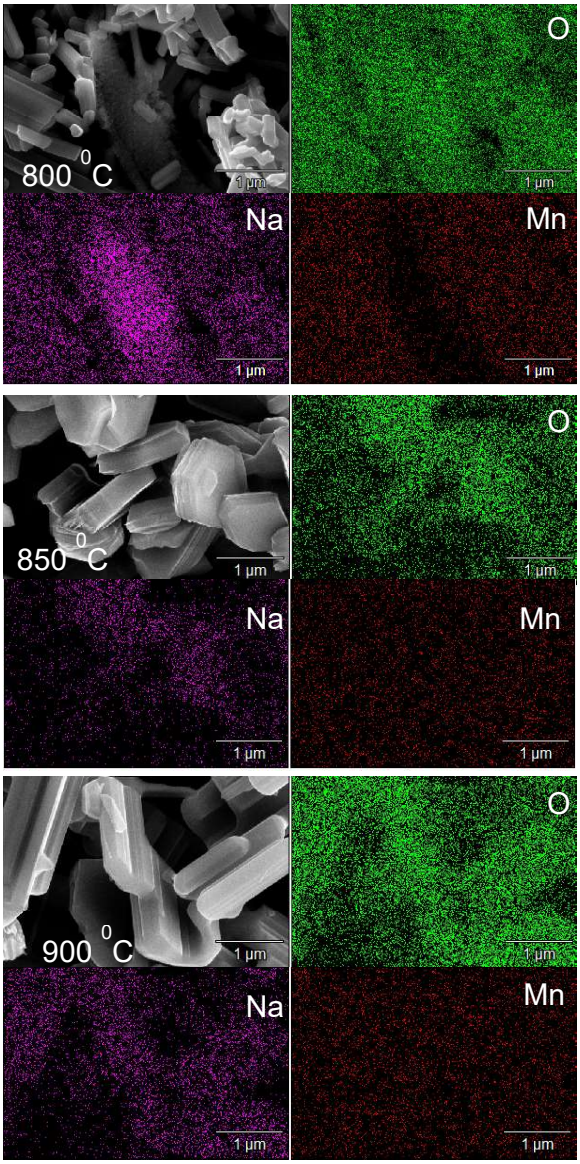

Fig. 2

Figure 3

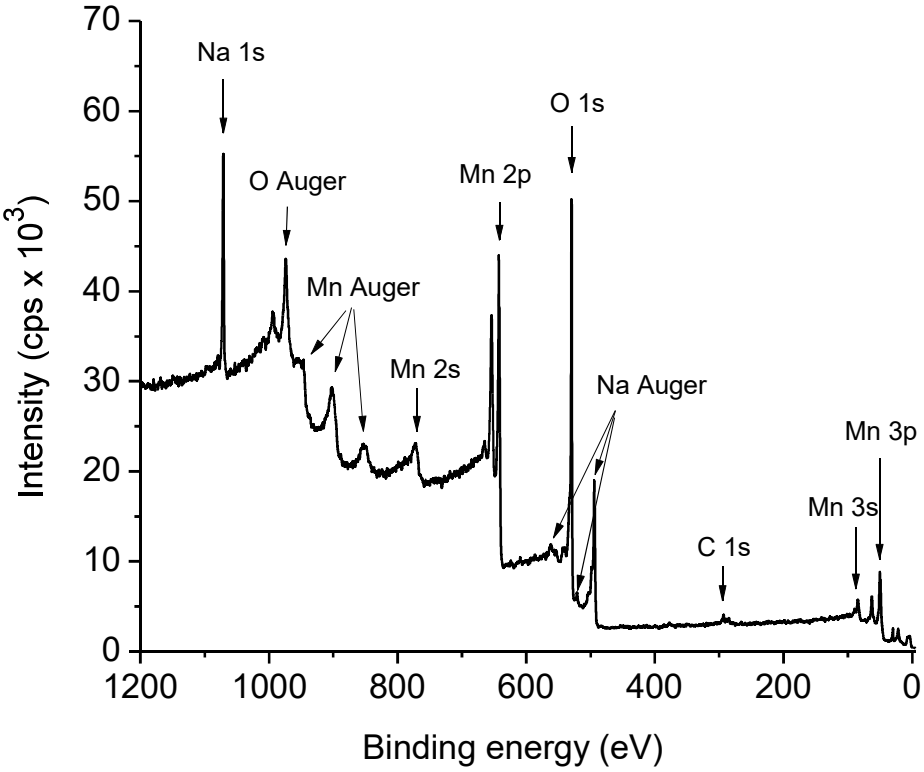

Fig. 3

Figure 4

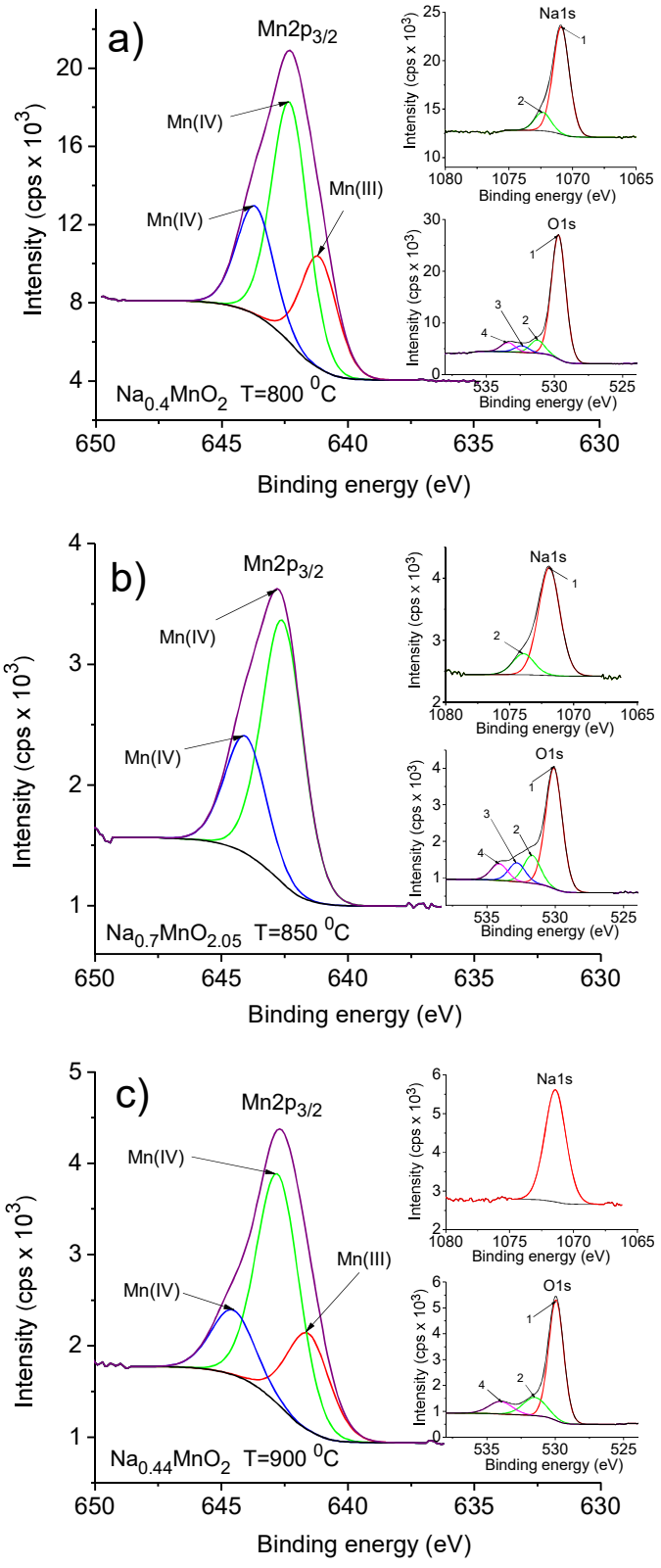

Fig. 4

Figure 5

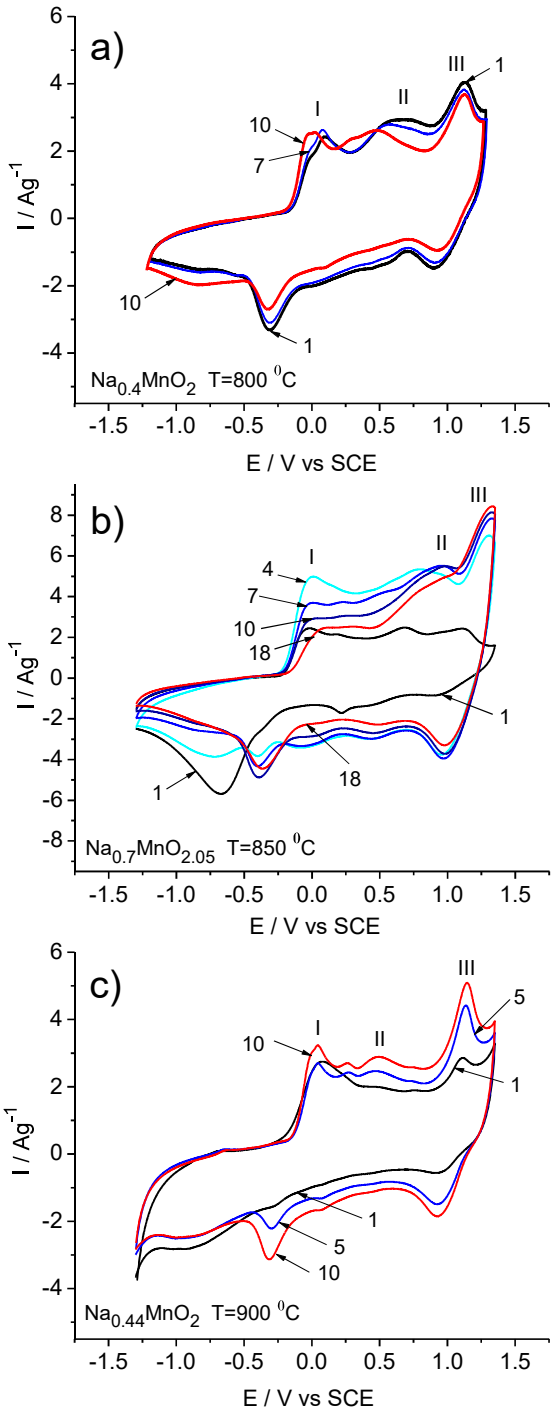

Fig. 5

Figure 6

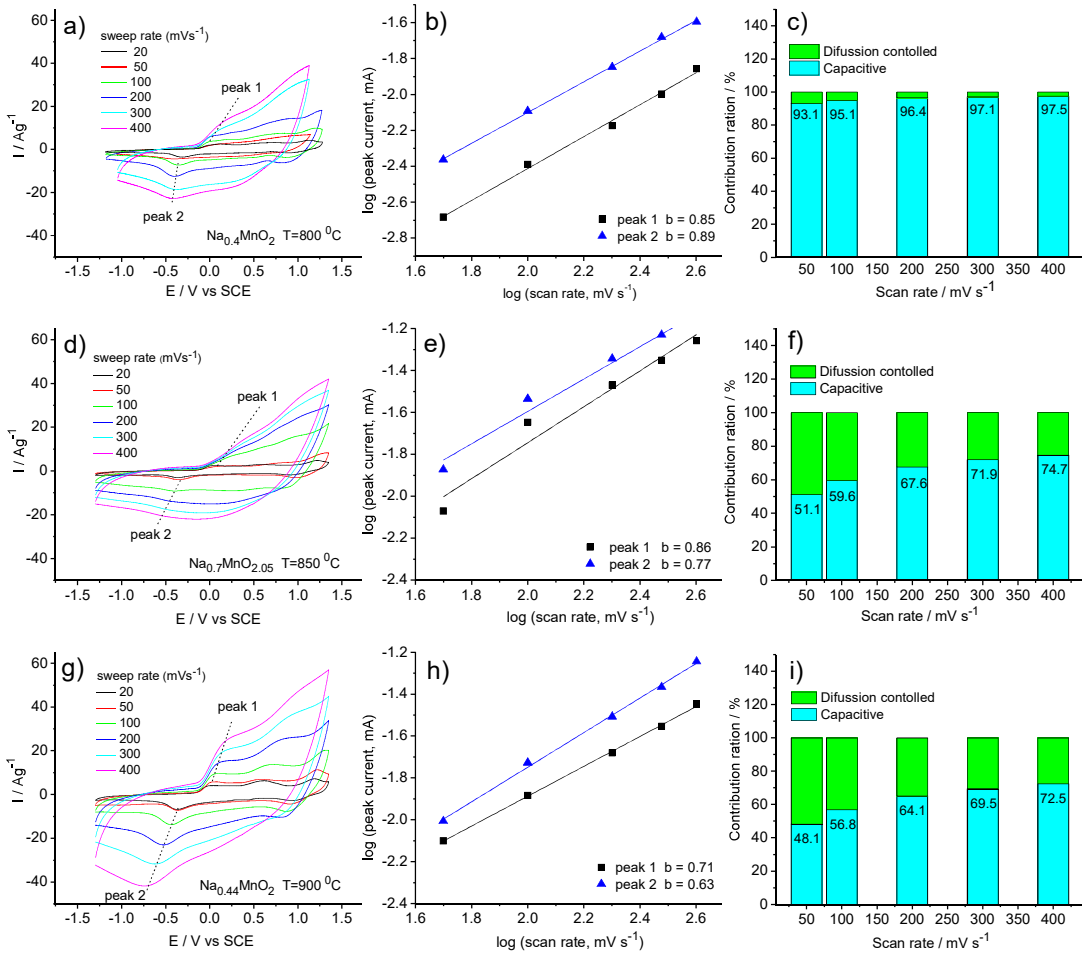

Fig. 6

Figure 7

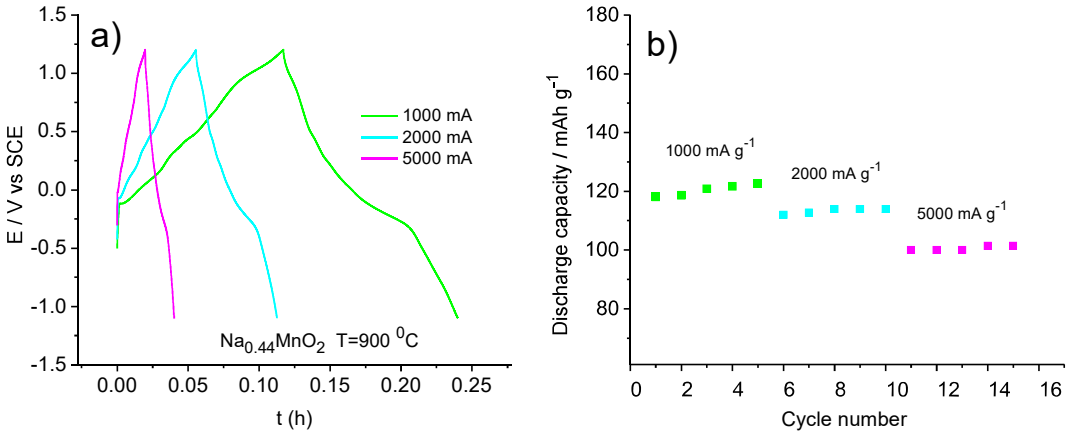

Fig. 7